Journal of Power Sources 195 (2010) 5185–5196

Contents lists available at ScienceDirect

Journal of Power Sources

journal homepage: www.elsevier.com/locate/jpowsour

On the role of ultra-thin oxide cathode synthesis on the functionality of micro-solid oxide fuel cells: Structure, stress engineering and *in situ* observation of fuel cell membranes during operation

Bo-Kuai Lai, Kian Kerman, Shriram Ramanathan*

Harvard School of Engineering and Applied Sciences, Harvard University, 29 Oxford St., Pierce Hall, Cambridge, MA 02138, USA

ARTICLE INFO

Article history:
Received 27 December 2009
Received in revised form 24 February 2010
Accepted 25 February 2010
Available online 3 March 2010

Keywords:
LSCF
Solid oxide fuel cell
Cathode
Thin film
Microstructure
Stress

ABSTRACT

Microstructure and stresses in dense $La_{0.6}Sr_{0.4}Co_{0.8}Fe_{0.2}O_3$ (LSCF) ultra-thin films have been investigated to increase the physical thickness of crack-free cathodes and active area of thermo-mechanically robust micro-solid oxide fuel cell (μSOFC) membranes. Processing protocols employ low deposition rates to create a highly granular nanocrystalline microstructure in LSCF thin films and high substrate temperatures to produce linear temperature-dependent stress evolution that is dominated by compressive stresses in μSOFC membranes. Insight and trade-off on the synthesis are revealed by probing microstructure evolution and electrical conductivity in LSCF thin films, in addition to *in situ* monitoring of membrane deformation while measuring μSOFC performance at varying temperatures. From these studies, we were able to successfully fabricate failure-resistant square μSOFC (LSCF/YSZ/Pt) membranes with width of 250 μm and crack-free cathodes with thickness of ~70 nm. Peak power density of ~120 mW cm^{-2} and open circuit voltage of ~0.6 V at 560 °C were achieved on a μSOFC array chip containing ten such membranes. Mechanisms affecting fuel cell performance are discussed. Our results provide fundamental insight to pathways of microstructure and stress engineering of ultra-thin, dense oxide cathodes and μSOFC membranes.

1. Introduction

Solid oxide fuel cells (SOFCs) [1] that are primarily made of thin films and created by microfabrication are an active area of research [2,3]. Such SOFCs, usually referred to as micro (μ) or thin-film (TF) SOFCs – (the former will be used throughout this article), hold tremendous potential for low temperature, low-cost SOFCs for portable energy [4]. In recent years, significant progress has been made on these devices – e.g., high power density at temperature below 500 °C [5–7] and low temperature synthesis of all μSOFC constituents [8–10] – and several μSOFC prototypes have been demonstrated [4–6,11,12]. The majority of μSOFCs reported to date use yttria-stabilized zirconia (YSZ) as the electrolyte and porous Pt as the anode, while porous Pt [5–6,13], $La_xSr_{1-x}CoO_3$ [11,14], and $La_xSr_{1-x}Co_yFe_{1-y}O_3$ (LSCF) [4,12] have been explored as the cathodes.

An increasing effort has been made to implement LSCF as the cathode for μSOFCs [4,6,12]. Due to its high mixed ionic and electronic conductivities and high electrocatalytic activity for oxygen reduction reaction, LSCF is considered a promising cathode material for intermediate-temperature SOFCs [15]. Our recent studies have shown that high-quality LSCF thin films can be synthesized by sputtering at relatively low temperatures, thus avoiding any interfacial reaction with YSZ electrolytes. In-plane electrical conductivity and its activation energy [8,10], as well as activation energy of surface area specific resistance [9] of the sputtered ultra-thin, nanocrystalline LSCF films are comparable to their macrocrystalline counterparts [15]. As detailed in our recent study [8], microstructure in sputtered LSCF thin films is strongly correlated to film thickness and thermal treatments. In order to prevent formation and propagation of cracks that could eventually lead to failure of μSOFC membranes, while maintaining adequate electrical conductivity, film thickness of sputtered LSCF needs to be precisely controlled in 15–30 nm range and annealing temperature needs to be lower than 550 °C [8]. However, the thickness limitation severely constrains the conductance of LSCF cathodes, which can lead to insufficient current supply and collection if no additional current collector [6,14] is employed. It has been reported that when Pt mesh is placed on top of the cathode, the power density of μSOFCs with 20-nm-thick LSCF increases by one order of magnitude [6]. In addition to oxide cathodes, another challenge for μSOFC advancement is the need to increase total power output for applications. In order to increase power output, it is essential to increase

* Corresponding author. Tel.: +1 617 496 0358; fax: +1 617 495 9837.
E-mail address: shriram@seas.harvard.edu (S. Ramanathan).

0378-7753/$ – see front matter © 2010 Elsevier B.V. All rights reserved.
doi:10.1016/j.jpowsour.2010.02.079

Table 1
List of LSCF thin films with their corresponding thickness, target power, and substrate temperature, as well as their appearances in this article and references.

LSCF thin-film ID	Thickness	Target power	Substrate temperature	Discussed in
80nm-150W-RT	80 nm	150 W	RT	Section 3.1
71nm-150W-RT	71 nm	150 W	RT	Section 3.1
65nm-20W-RT	65 nm	20 W	RT	Section 3.1
67nm-20W-RT	67 nm	20 W	RT	Section 3.1
71nm-150W-500C	71 nm	150 W	500 °C	Section 3.2
67nm-20W-500C	67 nm	20 W	500 °C	Section 3.2
60W-RT	9–63 nm	60 W	RT	Refs. [8,10,22]
60W-550C	15, 60, 150 nm	60 W	550 °C	Refs. [12,22]

active area for electrochemical reactions. The width or diameter of reported sub-μm free-standing μSOFC membranes with oxide cathodes [4,6,11,12] is in the range of 200 μm or less.

The goal of this report is to explore pathways to overcome the thickness limitation of LSCF cathodes and the area limitation of μSOFC membranes through microstructure and stress engineering in LSCF thin films. To achieve this goal, substrate temperature and deposition rate are varied in ~70-nm-thick LSCF thin films and temperature-dependent deformation patterns of $250 \pm 10\ \mu m^2$ membranes in μSOFC arrays are investigated. As suggested by the Thornton structure zone diagram [16,17], physical structure of sputtered thin films is determined by thermal- and bombardment-induced mobility of surface adatoms, lattice atoms, defects and flux of sputtering atoms at the growing film surface. High substrate temperature increases mobility of adatoms and defects, forming larger grains; while high deposition rate tends to produce dense microstructures as a result of energetic particle bombardment and limited diffusion length of surface adatoms during high-flux bombardment. Stresses in thin films are also affected by these factors and are highly dependent upon types of materials and film thickness. The use of μSOFC arrays enables a better assessment of the yield of μSOFC membranes after various processing steps and during testing.

In this article, we demonstrate that both LSCF thickness and μSOFC area can be simultaneously increased by optimizing deposition rate and substrate temperature. The mechanisms leading to these results will be discussed. The effect of deposition rate on microstructure and the effect of substrate temperature on stress evolution are emphasized in Sections 3.1 and 3.2, respectively. Through the improvement of microstructure and stresses in LSCF thin films, a peak power density of $\sim 120\ mW\ cm^{-2}$ and an OCV of ~0.6 V at 560 °C for 250 μm × 250 μm μSOFC membranes with 70-nm-thick LSCF cathode were achieved. We anticipate the results presented in this article could advance understanding of the complex high temperature behavior in thin, dense oxide cathode and μSOFC membranes.

2. Experimental

RF sputtering was carried out using custom $La_{0.6}Sr_{0.4}C_{0.8}F_{0.2}O_3$ (LSCF) and 8% yttria-stabilized zirconia (YSZ) targets (both from AJA International) at Ar pressure of 5 mTorr. Target power used for YSZ thin films was 60 W, yielding a nominal deposition rate of $\sim 1.2\ nm\ min^{-1}$. 20 W and 150 W of target power were used to deposit LSCF thin films and the corresponding nominal deposition rate was 0.3 and $2.9\ nm\ min^{-1}$, respectively. The various LSCF thin films discussed in this article are listed in Table 1 with their corresponding deposition parameters.

μSOFC arrays, with ten μSOFC membranes arranged in a circular fashion, were fabricated on the silicon nitride (SiN)-coated Si chips. Similar μSOFC arrays have been reported in Ref. [18]. The fabrication employed photolithography to pattern SiN thin films, reactive ion etching (RIE) to remove patterned SiN, and 30% KOH to etch through Si. After processing, ten SiN membranes were released from Si. YSZ and LSCF were then deposited onto the front side (i.e., the exposed side of SiN thin films prior to processing) of the SiN membranes, forming LSCF/YSZ/SiN membranes. Regardless of deposition conditions of YSZ and LSCF, the LSCF/YSZ/SiN, as well as SiN, membranes were flat (i.e., not buckled or no out-of-plane deformation). To accomplish LSCF/YSZ/Pt (LYP) μSOFC membranes, the SiN layer in LSCF/YSZ/SiN membranes was removed by reactive ion etching (RIE) from the back side, then porous platinum (Pt) with thickness of ~120 nm was sputtered at a DC power of 250 W and a pressure of 75 mTorr. Note that YSZ and LSCF were always deposited in the same sputtering session.

Annealing was carried out in ambient conditions in a Thermolyne 21100 tube furnace. Unless otherwise specified, annealing time at peak temperature was 2 h and ramping and cooling rates were $5\ °C\ min^{-1}$. Grazing incidence X-ray diffraction (XRD) and X-ray reflectivity were performed with a Scintag 2000 diffractometer using Cu Kα radiation. Prior to the X-ray measurements, rocking curve measurements were performed to ensure accurate alignment between the detector and X-ray tube. Surface morphology was investigated by Carl Zeiss Ultra 55 field emission scanning electron microscopy (SEM). Temperature-dependent film stresses were measured by a Toho FLX-2320-S thin film stress measurement system with 2 h of holding at 500 °C; the heating rate and cooling rate were $2\ °C\ min^{-1}$ and $5\ °C\ min^{-1}$ for wafers with amorphous and crystalline LSCF thin films, respectively. The system measured stress-induced curvature change of 4" substrate wafers prior to and after thin-film deposition. Film stresses were determined from the Stoney equation [19,20]. Nominal substrate thicknesses of 500 μm and biaxial modulus of 181 GPa for Si were used in the stress calculation.

High temperature lateral electrical conductivity and fuel cell measurements were performed using the same apparatus, whose details can be found elsewhere [12,21]. Thin films required for these two measurements were *concurrently* deposited onto their respective substrates. Samples for conductivity measurements were then sputtered with 220-nm-thick Pt strips on the opposite side of the samples using a 125-μm-thick stainless steel shadow mask. The Pt strips served as contact pads for micromanipulator probes with Pt-plated tungsten tips. To avoid Pt coating onto the side walls of testing samples, the dimensions of the Pt strips are 9.0 mm × 3.1 mm. The separation between Pt strips was 2.8 mm. In-plane current was measured over a voltage sweep from −10 to 10 mV, which took ~40 s to collect 50 data points. Linear regression of the current–voltage plots, which yields film resistance, was used to calculate in-plane conductivity of LSCF thin films. Temperature profile of the conductivity measurement was as follows: heating from room temperature (RT) to 200 °C at $5\ °C\ min^{-1}$ → heating from 200 °C to 450 °C at $2\ °C\ min^{-1}$ → holding at 450 °C for 30 min → heating from 450 °C to 550 °C at $1\ °C\ min^{-1}$ → holding at 550 °C for 30 min → cooling from 550 °C to RT at $2\ °C\ min^{-1}$. The holding steps at 450 °C and 550 °C were to monitor possible conductivity change due to crystallization and microstructure development (e.g., grain growth or crack formation), respectively.

For the fuel cell measurement, forming gas (wet 5% H_2/95% Ar) was fed to the anode on the bottom of the chips while the top was exposed to air. A micromanipulator probe was located at the center of the chips. Temperature profile of the fuel cell measurement was as follows: heating from RT to 560 °C at 1 °C min^{-1} → holding at 560 °C for ~30 min → cooling from 560 °C to RT at 2 °C min^{-1}. A CCD camera (AmScope MD900E) connected to a computer was used to capture images of membrane deformation at automated intervals.

3. Results and discussion

Four types of LSCF thin films deposited at two different target powers (i.e., 20 W and 150 W) and two different substrate temperatures (i.e., without heating and 500 °C) were systematically investigated (see Table 1). In Section 3.1, LSCF thin films deposited at 20 W and 150 W without substrate heating are discussed to emphasize the effect of deposition rate on microstructures in LSCF thin films and on μSOFC membranes. In Section 3.2, the effect of substrate temperature on stress evolution in LSCF thin films and μSOFC membranes is emphasized using the LSCF thin films deposited at 20 W and 150 W at a substrate temperature of 500 °C. Correlation between microstructure and stresses will also be discussed in Section 3.2.

3.1. Microstructure engineering through deposition rate

80-nm-thick and 65-nm-thick LSCF thin films were deposited onto 60-nm-thick nanocrystalline YSZ thin film-coated SiN/Si substrates at a gun power of 150 W and 20 W, respectively, without substrate heating. The films are denoted here as 80nm-150W-RT and 65nm-20W-RT LSCF thin films, respectively. After deposition, the films were then annealed at various temperatures and the corresponding XRD patterns, taken at RT after each annealing, are displayed in Fig. 1(a) and (b), respectively. As seen, as-deposited YSZ is crystalline while LSCF is amorphous. Despite the difference in deposition rate for these two LSCF thin films being nearly one order of magnitude, their crystallization temperature was in 400–450 °C range, consistent with the 60W-RT LSCF thin films in our previous studies [8,10,21].

To determine the crystallization temperature and behavior, electrical conductivity measurements were performed on 71nm-150W-RT and 67nm-20W-RT LSCF thin films. Fig. 2 shows temperature dependence of electrical conductivity for these two thin films. The thin films exhibited similar electrical behavior but differed noticeably in the magnitude of electrical conductivity (σ) and activation energy (E_a). As-deposited amorphous thin films possessed low electrical conductivity. At temperatures slightly below 450 °C, electrical conductivity started to deviate from a monotonic linearly increasing function. While at ~450 °C, electrical conductivity dramatically increased by two orders of magnitude, an indication of crystallization onset [21], and the time needed for the crystallization process to complete is similar for both LSCF thin films. The significant increase in conductivity at ~450 °C is due to establishment of long-range order of Co–O–Co bonds, on which polaron hopping takes place, when LSCF is in crystalline phase [10,15]. At 550 °C, no apparent difference in electrical conductivity was observed while holding the temperature for 30 min. During cooling, E_a in 550–200 °C range, as shown in the inset of Fig. 2, was 0.09 eV and 0.14 eV for 67nm-20W-RT and 71nm-150W-RT LSCF thin films, respectively.

Figs. 3 and 4 show the surface morphology of 71nm-150W-RT and 67nm-20W-RT LSCF thin films, respectively, after annealing at different temperatures. As seen in Figs. 3(a) and 4(a), prior to any post-deposition heat treatment, these two thin films exhibit distinctly different surface morphologies. The former exhib-

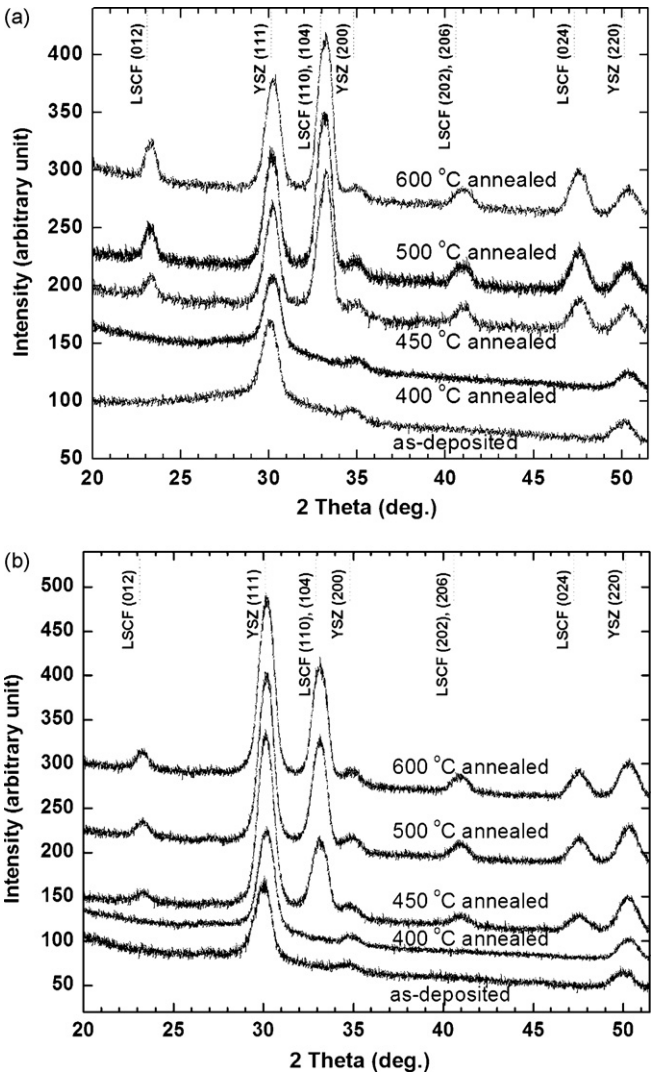

Fig. 1. XRD patterns of (a) 80nm-150W-RT and (b) 65nm-20W-RT LSCF thin films after various annealing temperatures.

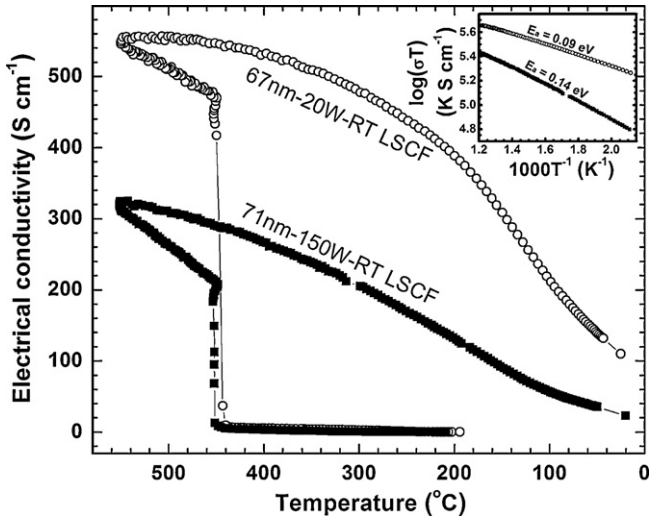

Fig. 2. Temperature dependence of electrical conductivity for 71nm-150W-RT (■) and 67nm-20W-RT (○) LSCF thin films. Corresponding Arrhenius plots of product of electrical conductivity and temperature in 550–200 °C range are shown in the inset.

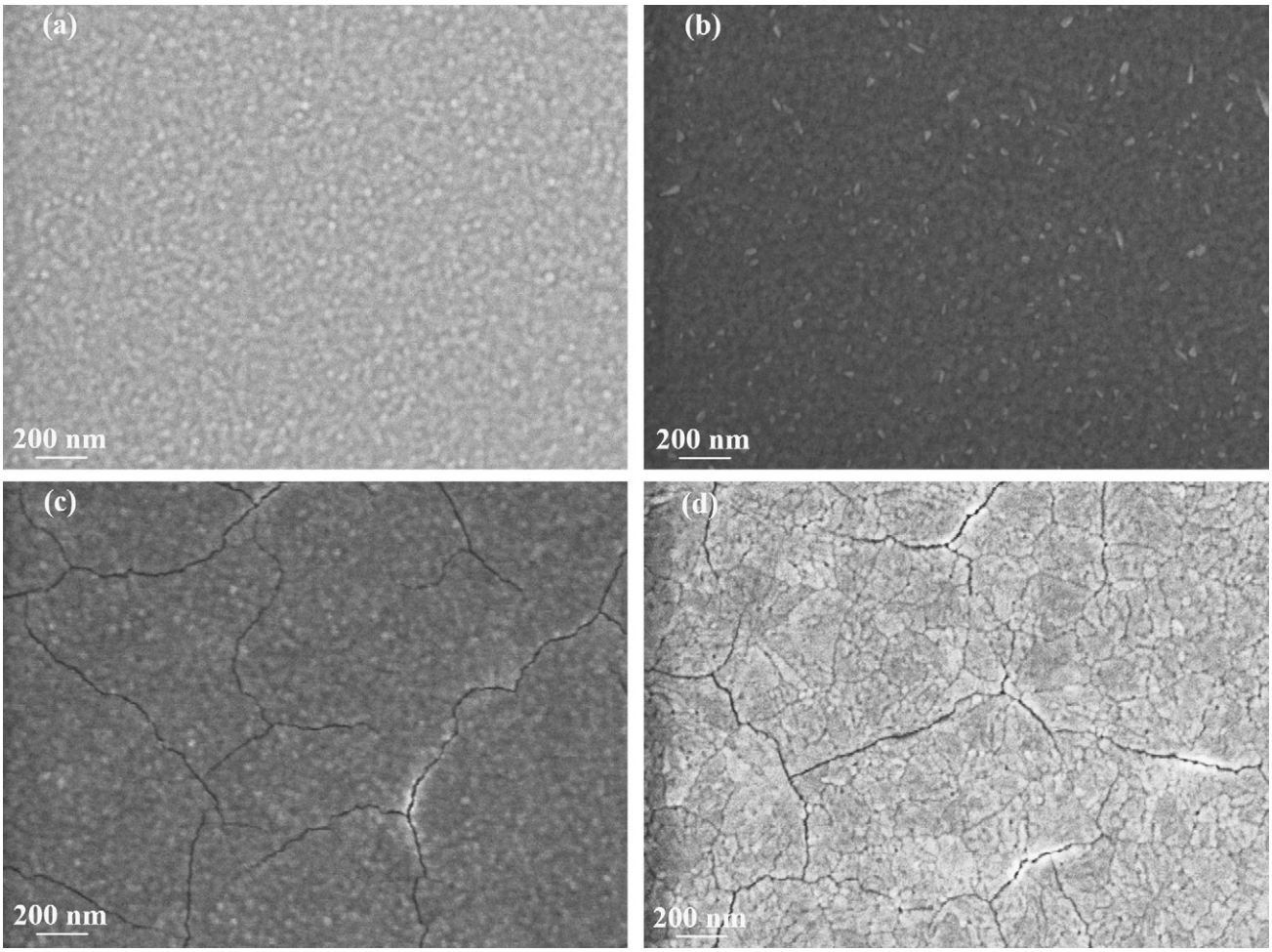

Fig. 3. 80nm-150W-RT LSCF thin films (a) prior to annealing and after annealing at (b) 450 °C, (c) 500 °C, and (d) 600 °C.

ited ultrafine nanocrystallinity, with very smooth surface and fine grains (<15 nm in diameter); while the latter showed highly granular nanocrystallinity, with congruent grains of similar size (25–35 nm). The ultrafine nanocrystalline microstructure in the 71-150W-RT LSCF thin films is likely due to inhibition of surface diffusion of adatoms by high flux of sputtering atoms. The structure remained similar when the films were annealed at 450 °C, as displayed in Fig. 3(b). However, after annealing at 500 °C (Fig. 3(c)), spatially extended channel cracks were formed in the 71-150W-RT LSCF thin films. This is due to the fact that for dense, well adhered continuous thin films, the strain energy is more easily relieved via formation of channel cracks, rather than other forms of cracks mentioned in Ref. [8]. After annealing at 600 °C (Fig. 3(d)), much larger grains, with irregular shape, and pinholes (only a few nm in diameter) at grain junctions were observed in addition to the channel cracks.

The granular nanocrystalline microstructure in the 67nm-20W-RT LSCF thin films is very stable, as seen in Fig. 4(a)–(d). After annealing at 450 °C (Fig. 4(b)), the grains were slightly larger in size when compared to those at RT (Fig. 4(a)). Apparent grain growth was observed in Fig. 4(c) for the 500 °C-annealed thin films. Traces of spatially confined channel cracks were also observed. However, these traces did not extend and connect to each other after annealing at 600 °C. Compared to the 60W-RT LSCF thin films that we have investigated [8,10], the 67nm-20W-RT LSCF thin films possessed the lowest E_a (0.09 eV) and the highest σ ($\sim$100 S cm^{-1}) at RT. In contrast, Figs. 2–4 clearly indicate that the lower σ and higher E_a in the 150W-RT LSCF thin films can be attributed to the higher level of material discontinuity (i.e., cracks) after they have crystallized.

The stress states in these two types of LSCF thin films were evaluated by their corresponding free-standing membranes, which were released from SiN using RIE, with width of $\sim$250 μm. As evident in the buckling patterns shown in Fig. 5(a) and (b), both thin films possessed compressive stresses. Compressive stresses have been observed in as-deposited YSZ thin films that were sputtered over a wide range of sputtering parameters [26]. Since compressive stresses are associated with adatom diffusion into grain boundaries [22,23], we speculate that oxygen vacancies in as-deposited LSCF and YSZ thin films might encourage diffusion of surface adatoms into grain boundaries. These may originate as a result of low oxygen partial pressure during deposition. In our previous studies [8], we have shown that RT-deposited LSCF thin films exhibit tensile stresses after annealing at 550 °C. Therefore, after annealing, the RT-deposited LSCF thin films experienced a change in stresses from compressive to tensile due to crystallization, oxygen uptake, and grain growth. Such compressive to tensile stress change has been reported for sputtered YSZ thin films [24].

μSOFC arrays with ten membranes based on these two types of LSCF thin films have been fabricated and tested. 60-nm-thick YSZ and 120-nm-thick porous Pt were used as the electrolyte and the anode, respectively. Accordingly, these two types of μSOFC arrays are referred to as 71nm-150W-RT LYP and 67nm-20W-RT LYP arrays. The width of the membranes was in 240–260 μm range. During fuel cell measurement, images of μSOFC membranes

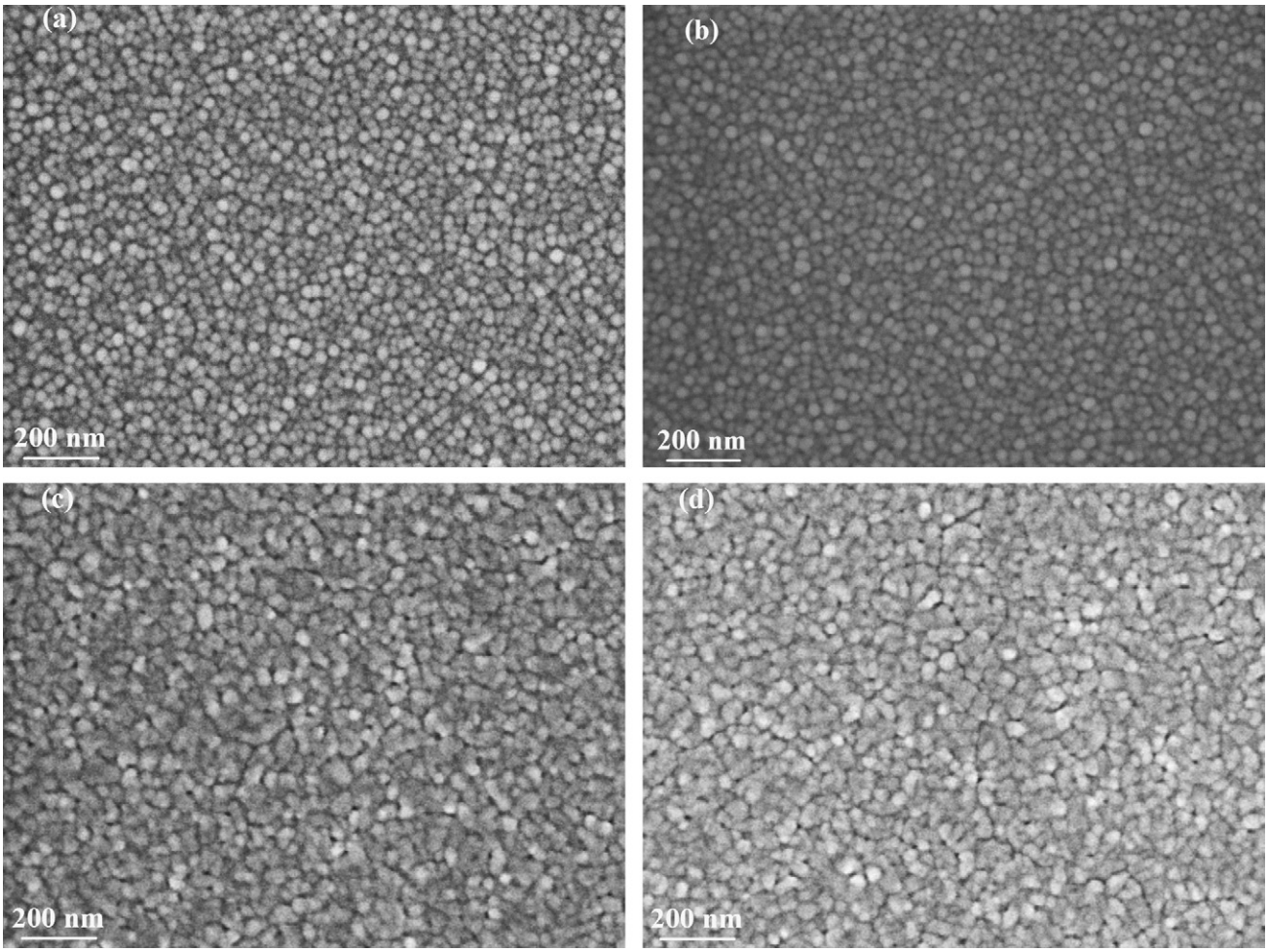

Fig. 4. 65nm-20W-RT LSCF thin films (a) prior to annealing and after annealing at (b) 450 °C, (c) 500 °C, and (d) 600 °C.

were continuously captured from a CCD camera-equipped stereo microscope. The micrographs at various temperatures are shown in Figs. 6 and 7 for selected membranes on the 71nm-150W-RT LYP and 71nm-150W-RT LYP arrays, respectively. Open circuit voltage (OCV) and peak power density (P_{max}), i.e., peak power divided by total area of functional membranes, of these two arrays are shown in Fig. 8.

As seen in Figs. 6(a) and 7(a), membranes in both arrays were buckled at RT, and the buckling was greater in the 71nm-150W-RT LYP array. During heating, the membranes in 71nm-150W-RT LYP array unbuckled at ~240 °C (Fig. 8(a)–(c)), buckled at ~270 °C (Fig. 8(d)–(f)), and unbuckled again at 420 °C (Fig. 8(g)–(i)). For the membranes in 67nm-20W-RT LYP array, they became unbuckled at ~100 °C (Fig. 8(a)–(c)), slightly buckled at ~410 °C (Fig. 8(e)), and then unbuckled again at ~430 °C (Fig. 8(f)). Since Pt and YSZ were identical for both LYP arrays, the results indicate that deformation evolution is highly associated with LSCF cathodes. It should be emphasized that μSOFC membranes with similar thickness do not necessarily have the same deformation processes. The exact deformation evolution in free-standing μSOFC membranes might

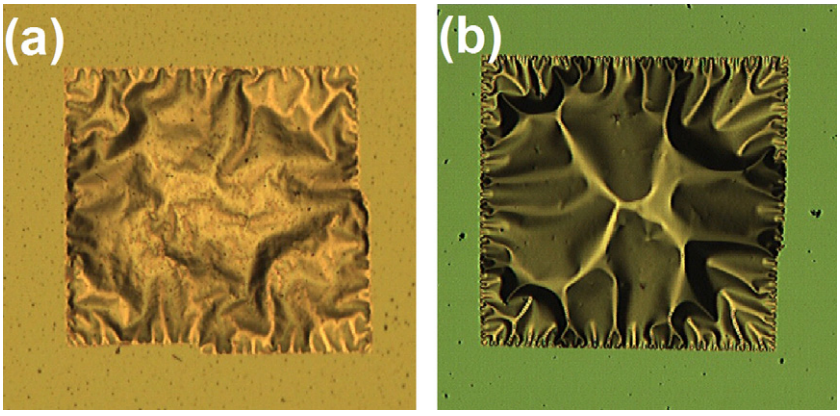

Fig. 5. Micrographs of (a) 80nm-150W-RT and (b) 65nm-20W-RT LSCF membranes, released from SiN thin films using reactive ion etching, with width of ~250 μm.

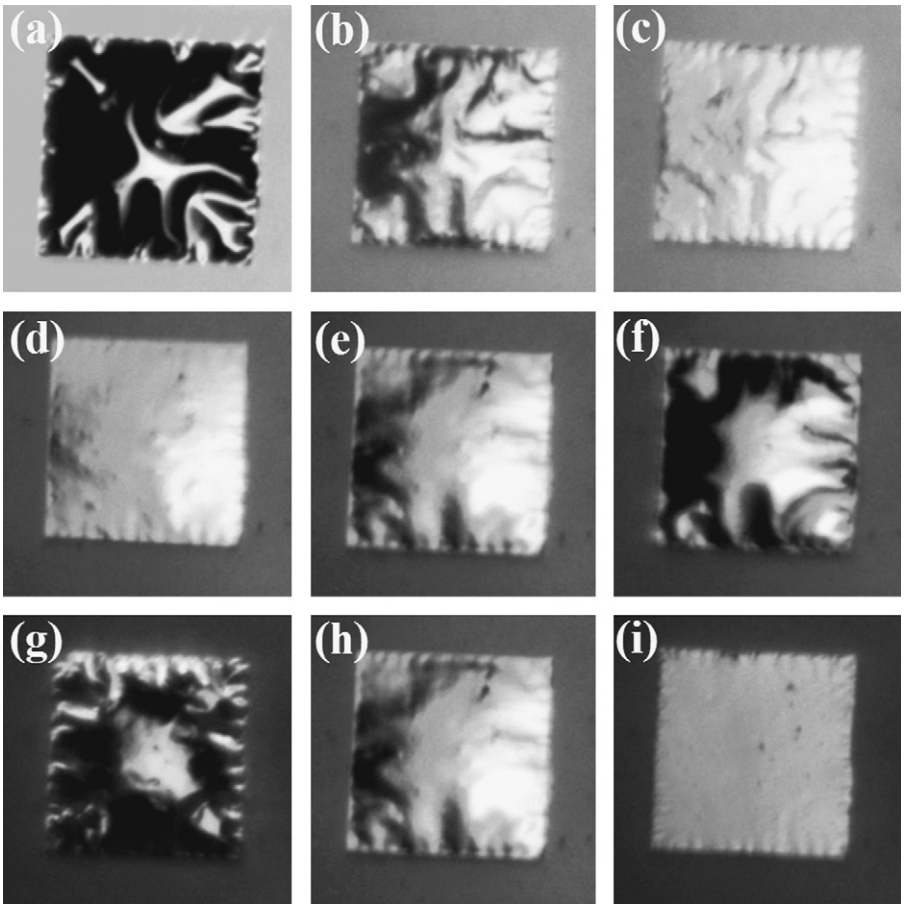

Fig. 6. Micrographs of 71nm-150W-RT LYP μSOFC membranes taken at (a) 20 °C, (b) 223 °C, (c) 238 °C, (d) 268 °C, (e) 270 °C, (f) 272 °C, (g) 412 °C, (h) 417 °C, and (i) 430 °C. Nominal width of the membranes is 250 μm.

depend on the competition between higher thermal expansion coefficients of LSCF, YSZ, and Pt, when compared to Si, (which tend to buckle membranes) and stress change towards tensile direction (which tends to flatten membranes). The unbuckling that occurred at ~425 °C for both arrays is probably due to the development of tensile stresses associated with crystallization of LSCF.

Fig. 8 shows temperature dependence of OCV and P_{max}; while the top inset shows percentage of intact μSOFC membranes (from

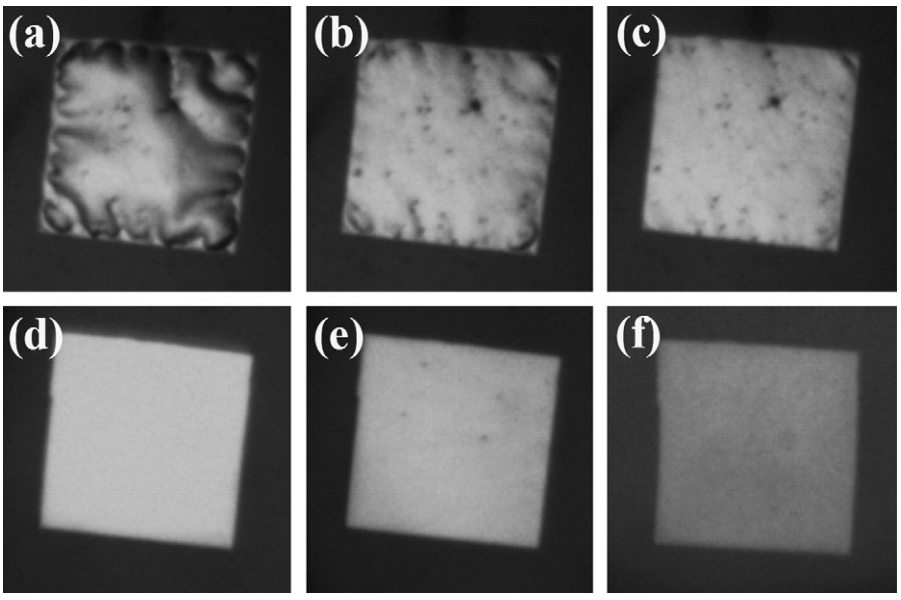

Fig. 7. Micrographs of 67nm-20W-RT LYP μSOFC membranes taken at (a) 20 °C, (b) 90 °C, (c) 100 °C, (d) 400 °C, (e) 407 °C (slightly buckled), and (f) 550 °C. Nominal width of the membranes is 250 μm.

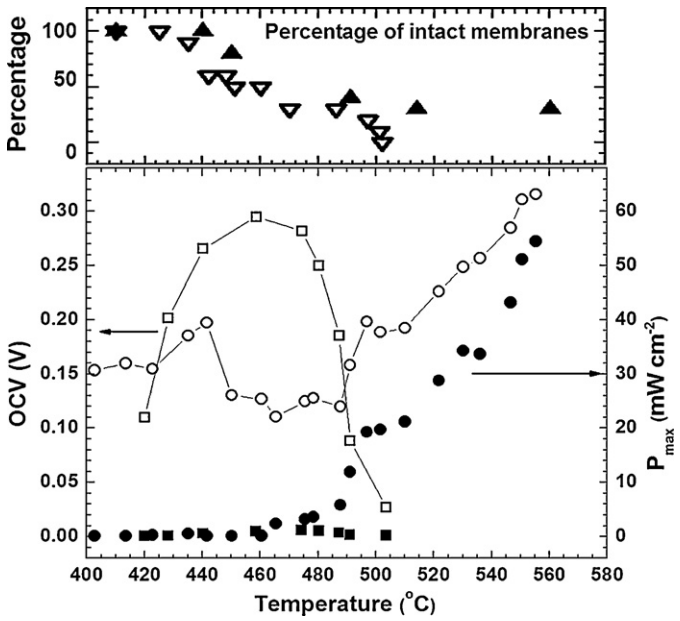

Fig. 8. Temperature dependence of open circuit voltage (OCV, open symbols) and peak power density (P_{max}, solid symbols) for 71nm-150W-RT LPY (circular symbols) and 67nm-20W-RT LPY (square symbols) μSOFC arrays. The inset shows percentage of non-broken μSOFC membranes as a function of temperature for 71nm-150W-RT LPY (▽) and 67nm-20W-RT LPY (▲) μSOFC arrays.

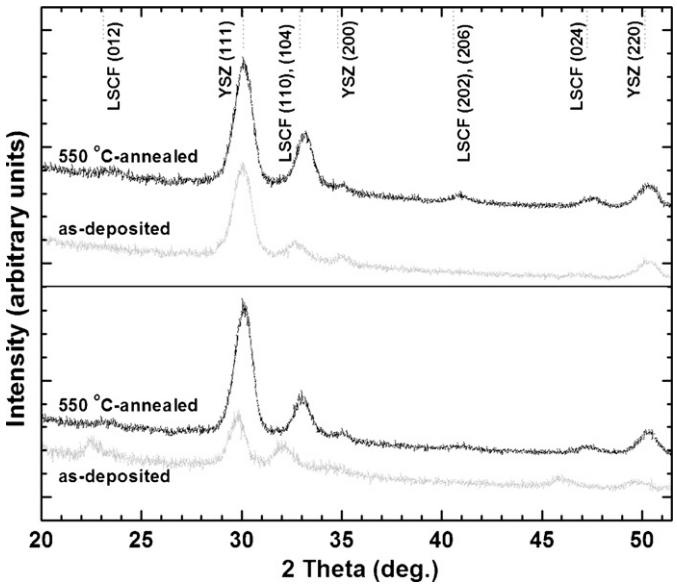

Fig. 9. XRD patterns of as-deposited (gray line) and 550 °C-annealed (black line) 71nm-150W-500C (lower panel) and 67nm-20W-500C (upper panel) LSCF thin films.

total of 40 membranes), as examined by microscopy, as a function of temperature. As seen, none of the membranes failed at temperatures below 420 °C in both arrays. However, as will be discussed later, OCV was still low, likely because of electrical leakage or fuel crossover. OCV of 71nm-150W-RT LYP array reached a maximum at 460 °C but its P_{max} did not exceed 1.5 mW cm^{-2}; and all the membranes failed at ~500 °C from visual observation. In comparison, OCV of 67nm-20W-RT LYP array started to increase above 450 °C when LSCF became crystalline. At 555 °C, their OCV and P_{max} reached ~0.32 V and ~55.0 mW cm^{-2}, respectively. Most of the membrane failure in 67nm-20W-RT LYP array occurred in 430–490 °C range. Since the membranes in both arrays became flat before crystallization onset (as seen in Figs. 6 and 7), crystallization- and grain growth-induced tensile stresses and the subsequent crack propagation are likely responsible for the failure.

3.2. Stress engineering by substrate temperature

The results in Section 3.1 show that, in addition to microstructure, stress engineering is also crucial to reduce membrane failure of μSOFCs. To avoid crystallization- and grain growth-related stress changes, LSCF thin films that are crystalline after deposition were sputtered at a substrate temperature of 500 °C. The high substrate temperature also pre-stabilizes the microstructure, making them more resistant to change during subsequent heating treatment. These two types of LSCF thin films are referred to as 71nm-150W-500C and 67nm-20W-500C LSCF thin films. The corresponding XRD patterns are shown in Fig. 9; while the corresponding surface morphologies are shown in Figs. 10(a) and 11(a), respectively. Temperature-dependent stress evolution in these two LSCF thin films together with 500 °C-deposited 60-nm-thick YSZ thin films (i.e., stress evolution in bilayer LSCF and YSZ thin films) are plotted in Fig. 12.

As seen in Figs. 9–11, both films are crystalline and exhibit similar surface morphology as their RT-deposited counterparts – namely, ultrafine nanocrystalline and highly granular nanocrystalline for the thin films deposited at a gun power of 150 W and

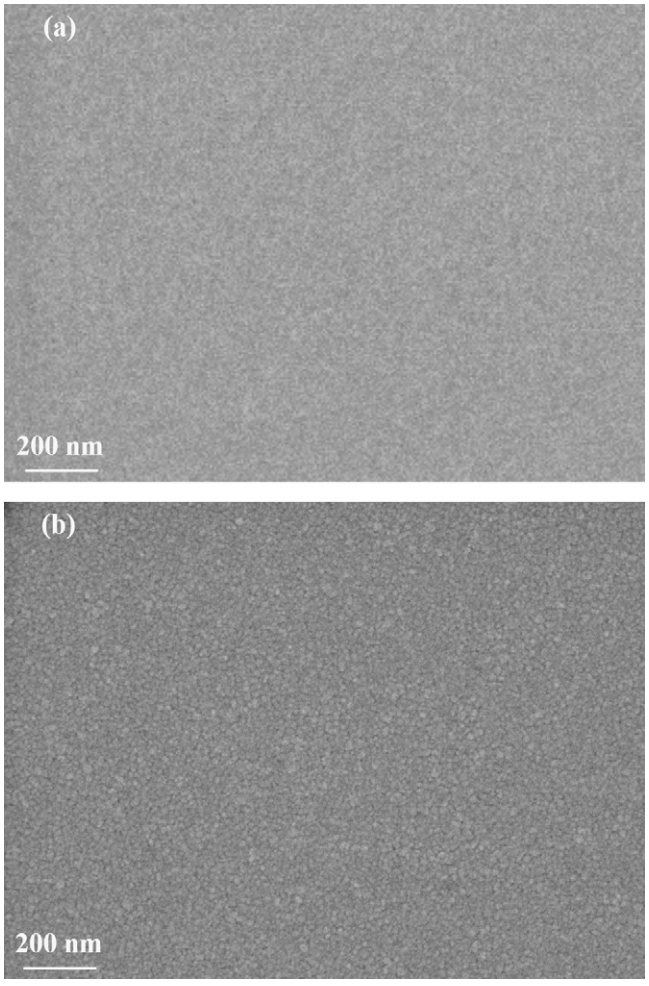

Fig. 10. SEM images of (a) as-deposited and (b) 550 °C-annealed 71nm-150W-500C LSCF thin films.

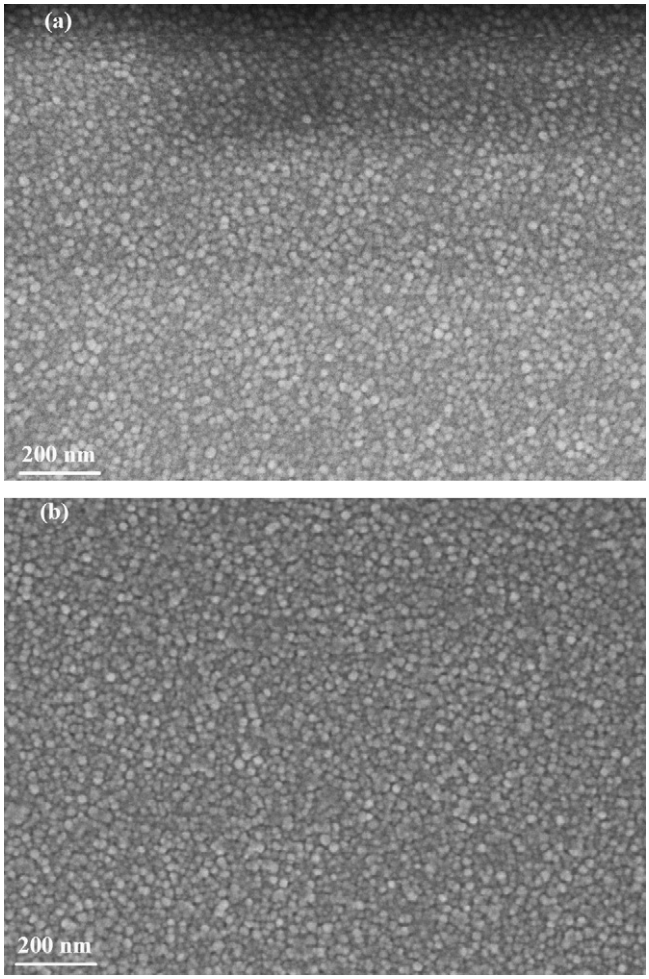

Fig. 11. SEM images of (a) as-deposited and (b) 550 °C-treated 67nm-20W-500C LSCF thin films.

20 W, respectively. As seen in Figs. 10(a) and 11(a), the grain size of these two 500 °C-deposited LSCF thin films was smaller than their RT-deposited counterparts (Figs. 3 and 4). The grain size of 67nm-20W-500C LSCF thin films is in 15–20 nm range. As will be discussed later, in addition to substrate temperature, compressive stresses are also responsible for the smaller grain size in the 500 °C-deposited LSCF thin films. Effect of treatment temperature on the microstructure of 71nm-150W-500C and 67nm-20W-500C LSCF thin films was examined after annealing at 550 °C. As seen in Fig. 10(b), no cracks were observed in the 71nm-150W-500C film after heating to 550 °C. This is likely due to the fact that the films were under compressive stress during the heat treatment, as seen in Fig. 12. No apparent morphology change was observed in the 550 °C-heat treated 67nm-20W-500C LSCF thin films (Fig. 11).

Fig. 12 shows that the difference between maximum and minimum stresses in a thermal cycle was ~600 MPa for both bilayer thin films. The stresses at RT in the as-deposited bilayer thin films with 71nm-150W-500C and 67nm-20W-500C LSCF were close to −40 MPa and −260 MPa, respectively, corresponding well to the deformation pattern of respective membranes displayed in the inset of Fig. 12. During heating, stresses in both bilayer thin films stabilized at temperatures in the vicinity of 400 °C and stress relaxation was observed when holding the temperature at 500 °C. During cooling, film stresses simply increased linearly with decreasing temperature, indicating their physical structures have been stabilized at 500 °C.

In addition to the differences in stress and structure evolution, several distinct differences were observed in XRD patterns of 500 °C-deposited crystalline LSCF thin films (Fig. 9) when compared to 500 °C-annealed RT-deposited LSCF thin films (Fig. 1). The differences include shift of positions towards lower 2θ for both primary LSCF (2θ = 32–33°) and YSZ (2θ = ~30°) peaks coupled with lower intensity and larger full width at half maximum (FWHM) of the primary LSCF peak. The lower 2θ is a result of higher lattice constant in oxygen-deficient LSCF thin films [15,25]; while the relatively low intensity and high FWHM are a result of higher level of oxygen defects, as well as by smaller grain size. Note that, as seen in Fig. 12, difference in film stresses between these two 500 °C-deposited films (~100 MPa) might not play a significant role on the shift in LSCF and YSZ peak positions. A more prominent peak shift and relatively high intensity of the LSCF peak at $2\theta \sim 23°$ was

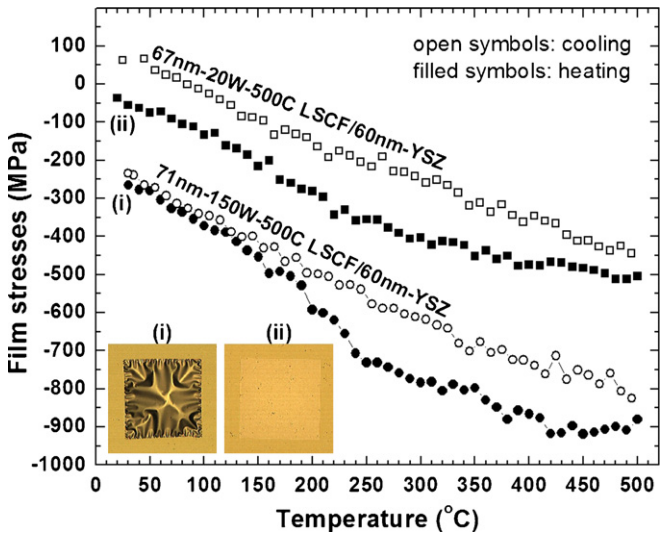

Fig. 12. Temperature dependence of film stresses in 71nm-150W-500C LSCF/60nm-YSZ and 67nm-20W-500C LSCF/60nm-YSZ bilayer thin films. Micrographs of the former and latter bilayer membranes, released from SiN thin films using reactive ion etching, taken prior to the measurement are shown in the insets (i) and (ii), respectively. Nominal width of the membranes is 250 μm.

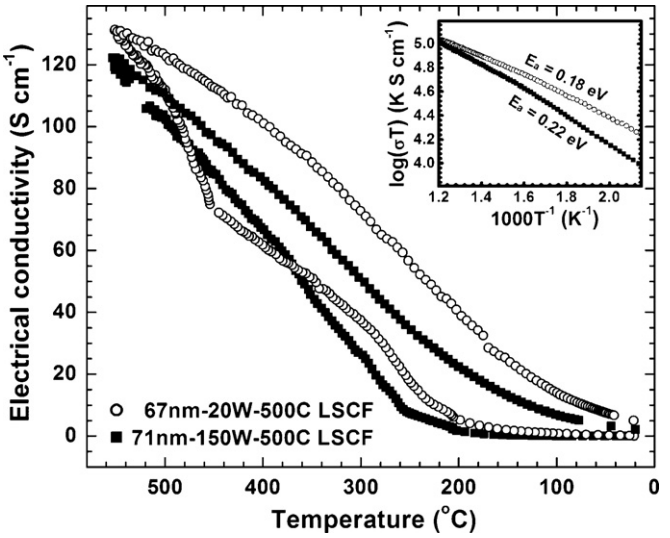

Fig. 13. Temperature dependence of electrical conductivity for 71nm-150W-500C (■) and 67nm-20W-500C (○) LSCF thin films. Corresponding Arrhenius plots of product of electrical conductivity and temperature in 550 – 200 °C range are shown in the inset.

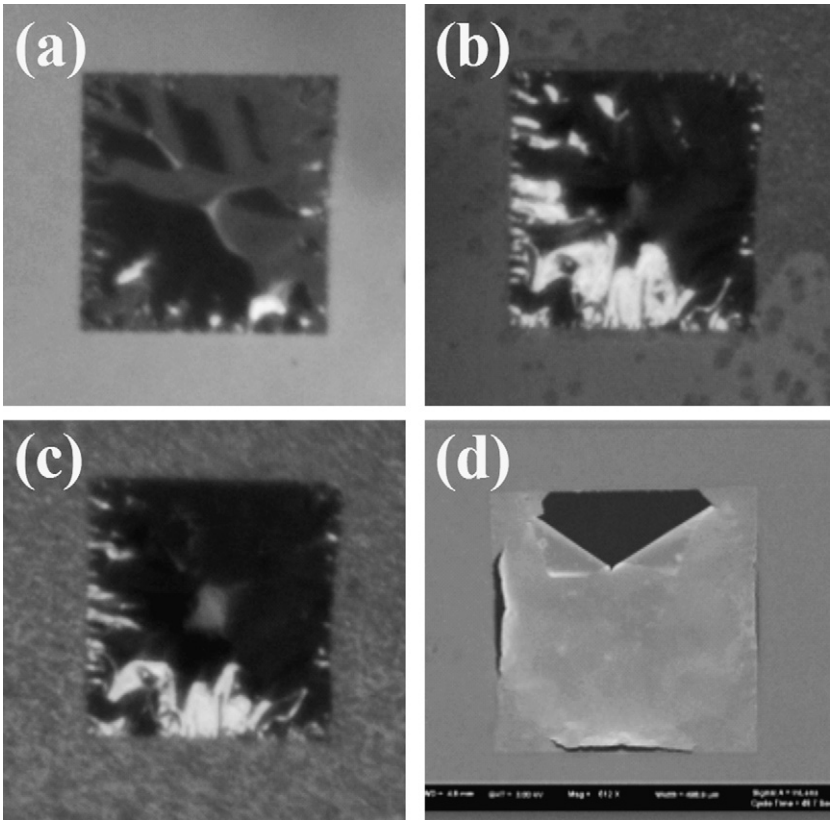

Fig. 14. Micrographs of 71nm-150W-500C LPY membranes taken at (a) 20 °C prior to the fuel cell measurement, (b) 495 °C during fuel cell measurement, and (c) 20 °C after the fuel cell measurement. (d) SEM image taken after fuel cell measurement.

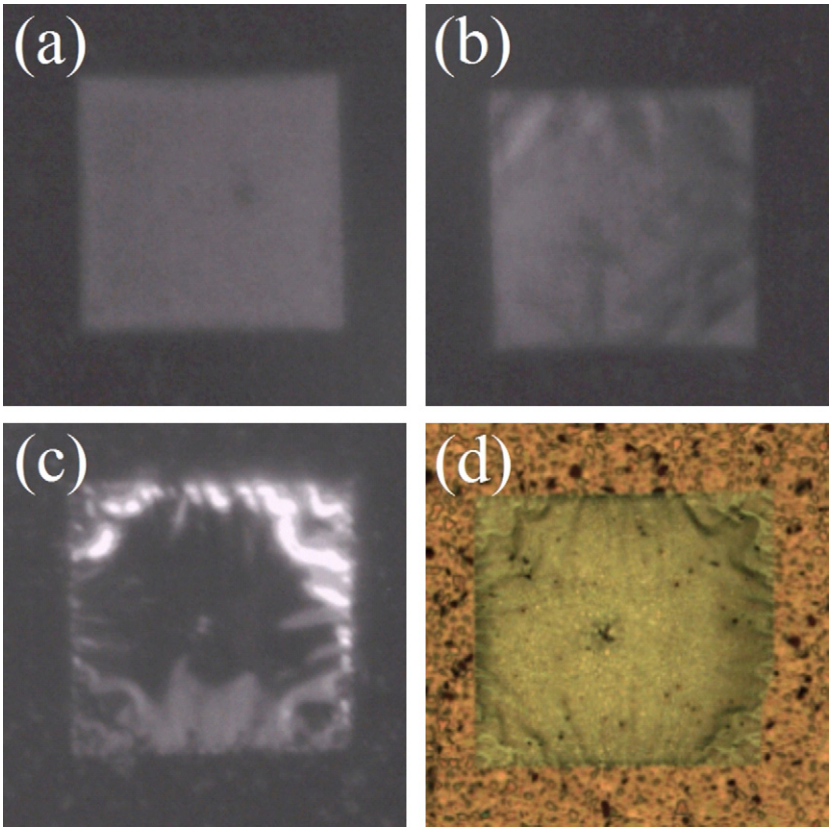

Fig. 15. Micrographs of 67nm-20W-500C LPY membranes taken at (a) 145 °C, (b) 150 °C, and (c) 430 °C during fuel cell measurement, and (d) 20 °C after the fuel cell measurement.

observed in the 71nm-150W-500C LSCF thin films. Although it could be due to the film texture with preferred orientation of rhombohedral LSCF (0 1 2) planes, one cannot rule out the possibility of cubic (JCPDS 01-089-5720) or orthorhombic (JCPDS 01-089-1267) phases in highly oxygen-deficient LSCF [25]. After 550 °C annealing in air, the primary LSCF peaks of both 500 °C-deposited LSCF thin films shifted to $2\theta \sim 33.0°$, as seen in Fig. 9, indicating a reduction in oxygen deficiency.

Temperature-dependent electrical conductivity of 71nm-150W-500C and 67nm-20W-500C LSCF thin films is plotted in Fig. 13. Although both thin films are crystalline, they exhibited low electrical conductivity below 200 °C. Together with Figs. 9–11, it is evident that the low conductivity is associated with oxygen deficiency, rather than microstructure. The increase in conductivity at ~200 °C for both as-deposited LSCF thin films is likely associated with increased activity of polaron transport and oxygen uptake. The latter can reduce the number of oxygen vacancies and thus, increase the number of polarons [25] leading to a conductivity increase with temperature. Since both thin films were already crystalline, no trace of crystallization-related conductivity jump was observed at 450 °C. At 550 °C, σ of 71nm-150W-500C LSCF thin films only reached 120 S cm^{-1} and E_a in 550 – 200 °C range during cooling was 0.22 eV; while σ and E_a for 67nm-20W-500C LSCF thin films were 130 S cm^{-1} and 0.18 eV, respectively. Compared to their RT-deposited counterparts (Fig. 2), the relatively low σ and relatively high E_a of 550 °C-treated 71nm-150W-500C and 67nm-20W-500C LSCF thin films are primarily due to their small grain size. Our previous studies have shown that conductivity in crack-free LSCF thin films is proportional to grain size [10]. Lower σ was also observed in 550 °C-treated 60nm-60W-550C LSCF thin films when compared to 550 °C-annealed 60nm-60W-RT LSCF thin films [21]. It is noted that compressive stresses may enhance conductivity because of reduction in polaron hopping distance along Co–O–Co bonds [26–29]. However, as seen in Figs. 1 and 9, the stresses at RT in 550 °C-annealed 67nm-20W-500C LSCF thin films did not lead to apparent difference in lattice constant when compared to 550 °C-treated 67nm-20W-RT LSCF thin films.

Figs. 14 and 15 show representative membranes in 71nm-150W-500C and 67nm-20W-500C LYP arrays, respectively, at various temperatures during fuel cell testing. Performance of the μSOFCs arrays is shown in Fig. 16. As seen in Figs. 12, 14(a) and 15(a), both thin films retained their respective stress states after Pt deposition. Deformation evolution of the membranes qualitatively corresponds to the trend of stress evolution well (Fig. 12). The membranes in the 71nm-150W-500C LYP array remained buckled (Fig. 14(b)) at temperatures all the way up to 560 °C, as well as after cooling down to RT (Fig. 14(c)). None of the ten membranes in the 71nm-150W-500C LYP array failed immediately after the testing. However, after careful examination by SEM (Fig. 14(d)), the membranes were found to exhibit cracking around the center of each side. Such cracking patterns were developed due to stress concentration, which is more prominent around the center of each side than around the corner, when the membranes were buckled under considerable compressive stresses.

For the membranes in 67nm-20W-500C LYP array, they became buckled at ~150 °C (Fig. 15(b)). The buckling gradually developed with increasing temperature (as seen in Fig. 15(c)) and persisted at RT after the testing (Fig. 15(d)). Overall, the buckling was not as severe as the membranes in 71nm-150W-500C LYP array and no cracks were observed at the perimeter of the membranes, as seen in Fig. 16(a).

The performance of 71nm-150W-500C LYP and 67nm-20W-500C LYP arrays are shown in Fig. 17. As seen in Fig. 17(a), the OCV of 71nm-150W-500C LYP array was below 0.1 V at 400 °C. It began to increase at ~450 °C and reached its maximum, 0.46 V, at ~545 °C; while the peak power density began to increase at ~490 °C and reached 75 mW cm^{-2} at ~560 °C. Voltage and power density as a function of current density for the 71nm-150W-500C LYP array at selected temperatures is shown in Fig. 17(b). For 67nm-20W-500C LYP array, higher OCV (~0.38 V) and higher peak power density (~20 mW cm^{-2}) were observed at 400 °C. The OCV and peak power density then increased gradually until reaching their maximum of 0.6 V and 120 mW cm^{-2}, respectively, at ~560 °C. Voltage and power density as a function of current density for the 67nm-20W-500C LYP array at selected temperatures is shown in Fig. 17(c). The peak power density of 67nm-20W-500C LYP array at 500 °C is similar (~60 mW cm^{-2}) to the single-cell μSOFCs in our recent report [12], despite having a lower OCV (0.5 V vs. 1.0 V).

Finally, we discuss the lower OCV in the μSOFC arrays observed in this study. First, we note that oxide cathode-based micro or thin-film SOFCs reported in the literature [4,11,14] usually exhibit OCV lower than its ideal value of ~1.0 V at high temperatures. The first mechanism limiting OCV is fuel crossover through pores or cracks in the electrolyte. This reduces the chemical gradient, and thus the corresponding voltage via chemical reaction, across the electrolyte. The existence of cracks is evident in Fig. 16(b). The second mechanism is the electronic leakage currents through the electrolyte. The third mechanism is probably the resistive loss from oxide cathodes. A slightly higher OCV has been observed when Pt mesh is used in contact with LSCF cathode during fuel cell measurement [6]. The former two mechanisms are active even if current flow through the external load is absent and, thus, can lead to reduced voltage when the SOFC system is held at open circuit.

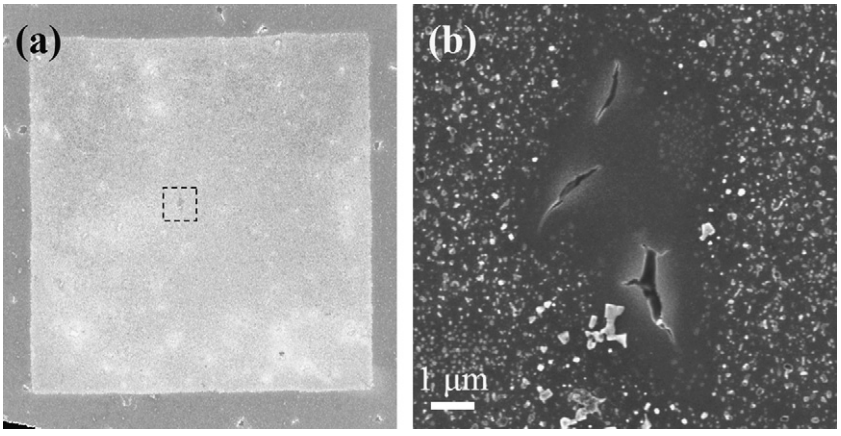

Fig. 16. (a) SEM image of a membrane in the 67nm-20W-500C LPY μSOFC array after fuel cell measurement. (b) Close up image of the selected region in (a).

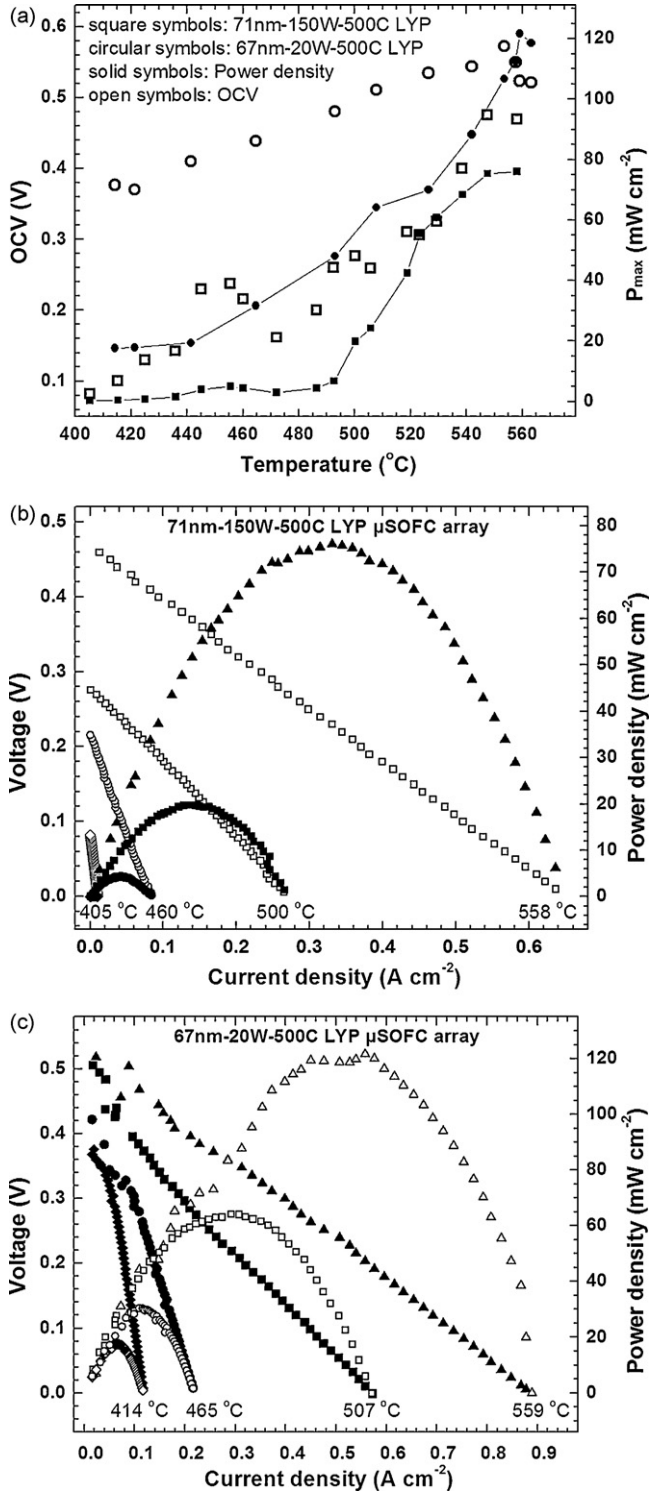

Fig. 17. (a) Temperature dependence of open circuit voltage (OCV, open symbols) and peak power density (P_{max}, solid symbols) for 71nm-150W-500C LYP (square symbols) and 67nm-20W-500C LYP (circular symbols) μSOFC arrays. Voltage (open symbols) and power density (solid symbols) as a function of current density at selected temperatures for (b) 71nm-150W-500C and (c) 67nm-20W-500C LYP μSOFC arrays.

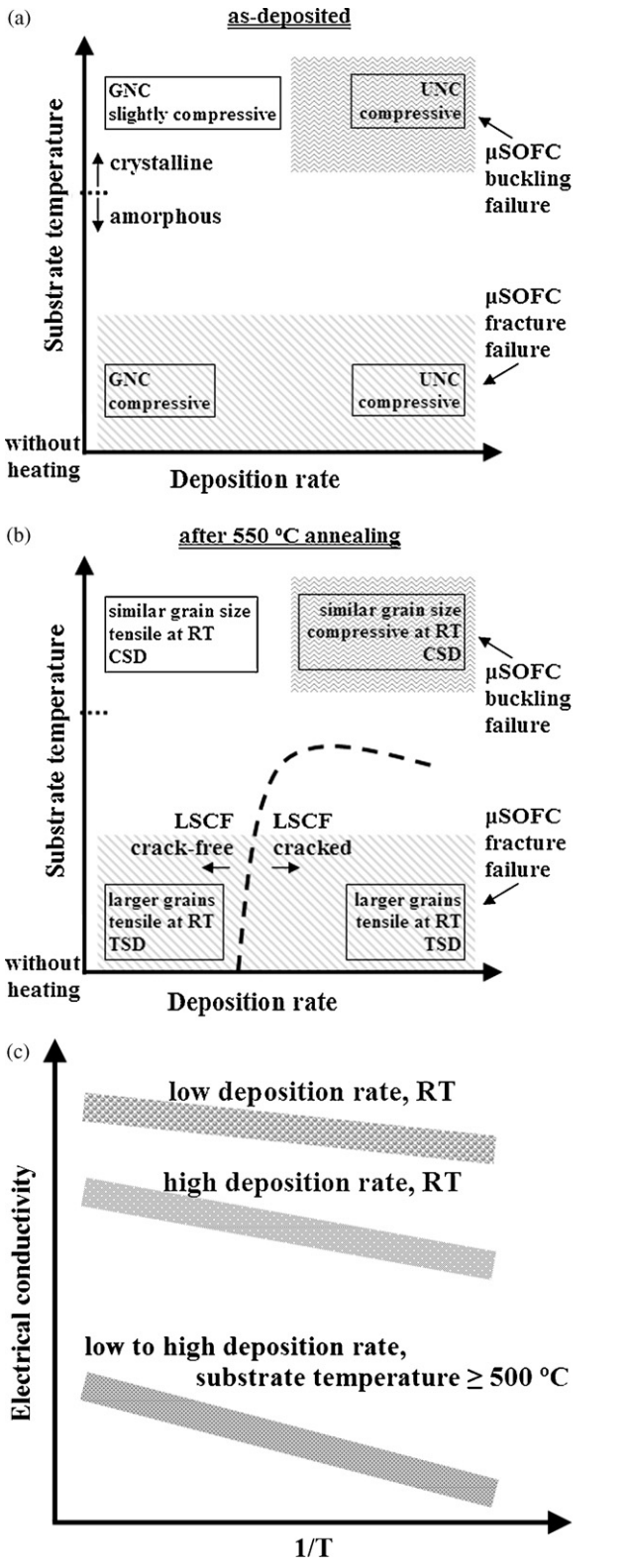

Fig. 18. (a) Microstructures and stresses in as-deposited 70-nm-thick LSCF thin films as a function of substrate temperature and deposition rate. UNC and GNC refer to ultrafine nanocrystalline and highly granular nanocrystalline microstructures, respectively. (b) Change in microstructures and stresses after annealing at 550 °C. Regions in the parameter space where buckling and fracture failures take place are also indicated. TSD and CSD refer to tensile stress-dominated and compressive stress-dominated stress evolution in LSCF thin films, respectively. (c) Effect of deposition rate and substrate temperature on electrical conductivity in 550 °C-annealed LSCF thin films.

From results presented here and our previous studies on 60W-RT and 60W-550C LSCF thin films [8,10,12,21], microstructures and stresses in as-deposited LSCF thin films with similar thickness in the substrate temperature and deposition rate parameter space are illustrated in Fig. 18(a); while the change in microstructures and stresses when the LSCF thin films are annealed at 550 °C are illustrated in Fig. 18(b). TSD and CSD refer to tensile stress- and compressive stress-dominated stress evolution, respectively. The failure modes for 250-μm-wide, free-standing μSOFC membranes with 70-nm-thick LSCF thin-film cathodes are also indicated in the figures. Effect of deposition rate and substrate temperature on temperature-dependent electrical conductivity in the 550 °C-treated LSCF thin films is illustrated in Fig. 18(c). As one can see, thermomechanical stability and performance of free-standing μSOFC membranes are strongly correlated to the microstructure and stress evolution in LSCF thin films. Although the LSCF thin films deposited at high temperature and low deposition rate provide the best thermomechanical stability and performance to the μSOFCs, they possess lower electrical conductivity because of smaller grain size. These figures provide insights into competing factors one may need to consider when synthesizing ultra-thin fuel cell components or devices.

4. Conclusions

In this article, microstructure and stress engineering have been explored for LSCF thin-film cathodes by varying sputtering deposition conditions. Insights into the mechanisms were probed by temperature-dependence of crystallization behavior, microstructure development, electrical conductivity in LSCF thin films, as well as high temperature deformation of μSOFC membranes. The primary results are summarized below:

1. LSCF thin films deposited at a high rate (target power = 150 W) and without substrate heating exhibited ultrafine nanocrystallinity, with very smooth surface and fine grains (<15 nm in diameter); while LSCF thin films deposited at low rate (target power = 20 W) and without substrate heating were granular, with grain size in 25–35 nm range. After annealing, the latter microstructure is more resistant to cracks.
2. Bilayer LSCF–YSZ thin films deposited at 500 °C possessed compressive stresses at RT and exhibited linear temperature-dependent stress evolution. No cracks were observed in the LSCF thin films up to 550 °C.
3. Electrical conductivity and activation energy are sensitive to details of microstructure and stress states in LSCF thin films. Superior electrical conduction properties of $\sigma \sim 550\,S\,cm^{-1}$ at 550 °C and $E_a = 0.09$ V in 550–200 °C range were observed for the LSCF thin films deposited at low rate without substrate heating.
4. Through exploring the processing protocols discussed above, we were able to fabricate failure-resistant μSOFCs (LSCF/YSZ/Pt) membranes with width of 250 μm and crack-free cathode films with thickness of ~70 nm. Peak power density of $\sim 120\,mW\,cm^{-2}$ and open circuit voltage of 0.6 V at 560 °C was achieved on a μSOFC array chip containing ten such membranes.

The results could be of potential relevance towards further advancing process science and technology of micro-solid oxide fuel cells utilizing thin film components.

Acknowledgments

The authors acknowledge SiEnergy Systems, National Science Foundation and Harvard SEAS for financial support.

References

[1] S.C. Singhal, K. Kendall, High Temperature Solid Oxide Fuel Cells: Fundamentals. Design and Applications, Elsevier, Oxford, UK, 2003.
[2] A.F. Jankowski, J.P. Hayes, R.T. Graff, J.D. Morse, Mater. Res. Soc. Symp. Proc. 730 (2002), V4. 2.1.
[3] S.J. Litzelman, J.L. Hertz, W. Jung, H.L. Tuller, Fuel Cells 8 (2008) 294–302.
[4] A. Bieberle-Hutter, D. Beckel, A. Infortuna, U.P. Muecke, J.L.M. Rupp, L.J. Gauckler, S. Rey-Mermet, P. Muralt, N.R. Bieri, N. Hotz, M.J. Stutz, D. Poulikakos, P. Heeb, P. Muller, A. Bernard, R. Gmur, T. Hocker, J. Power Sources 177 (2008) 123–130.
[5] H. Huang, M. Nakamura, P.C. Su, R. Fasching, Y. Saito, F.B. Prinz, J. Electrochem. Soc. 154 (2007) B20–B24.
[6] X.R. Jiang, H. Huang, F.B. Prinz, S.F. Bent, Chem. Mater. 20 (2008) 3897–3905.
[7] P.-C. Su, C.-C. Chao, J.H. Shim, R. Fasching, F.B. Prinz, Nano Lett. 8 (2008) 2289–2292.
[8] B.K. Lai, H. Xiong, M. Tsuchiya, A.C. Johnson, S. Ramanathan, Fuel Cells 9 (2009) 699–710.
[9] H. Xiong, B.-K. Lai, A.C. Johnson, S. Ramanathan, J. Power Sources 193 (2009) 589–592.
[10] B.-K. Lai, A.C. Johnson, H. Xiong, S. Ramanathan, J. Power Sources 186 (2009) 115–122.
[11] A. Ignatiev, X. Chen, N.J. Wu, Z.G. Lu, L. Smith, Dalton Trans. 40 (2008) 5501–5506.
[12] A.C. Johnson, B.-K. Lai, H. Xiong, S. Ramanathan, J. Power Sources 186 (2009) 252–260.
[13] X.H. Wang, H. Huang, T. Holme, X. Tian, F.B. Prinz, J. Power Sources 175 (2008) 75–81.
[14] S. Rey-Mermet, P. Muralt, Mater. Res. Soc. Symp. Proc. 972 (2007), AA07-10-BB08-10.
[15] L.-W. Tai, M.M. Nasrallah, H.U. Anderson, D.M. Sparlin, S.R. Sehlin, Solis State Ionics 76 (1995) 259–271.
[16] J.A. Thornton, Annu. Rev. Mater. Sci. 7 (1977) 239–260.
[17] R.A. Messier, P. Giri, R.A. Roy, J. Vac. Sci. Technol. A 2 (1984) 500–503.
[18] M. Tsuchiya, B.-K. Lai, A.C. Johnson, S. Ramanathan, J. Power Sources 195 (2010) 994–1000.
[19] B.-K. Lai, H. Kahn, S.M. Phillips, Z. Akase, A.H. Heuer, J. Mater. Res. 19 (2004) 2822–2833.
[20] F. Spaepen, Acta Mater. 48 (2000), 31–42, 21.
[21] T. Cain, B.-K. Lai, S. Sankaranarayanan, S. Ramanathan, J. Power Sources 195 (2010) 3145–3148.
[22] C.-W. Pao, S.M. Foiles, E.B. Webb, D.J. Srolovitz, J.A. Floro, Phys. Rev. Lett. 99 (2007) 036102.
[23] J.S. Tello, A.F. Bower, E. Chason, B.W. Sheldon, Phys. Rev. Lett. 98 (2007) 216104.
[24] D.J. Quinn, B. Wardle, S.M. Spearing, J. Mater. Res. 23 (2008) 609–618.
[25] S. Wang, M. Katsuki, M. Dokiya, T. Hashimoto, Solid State Ionics 159 (2003) 71–78.
[26] T.Y. Koo, S.H. Park, K.-B. Lee, Y.H. Jeong, Appl. Phys. Lett. 71 (1997) 977.
[27] X.J. Chen, S. Soltan, H. Zhang, H.-U. Habermeier, Phys. Rev. B 65 (2002) 174402.
[28] C.A. Perroni, V. Cataudella, G.D. Filippis, G. Iadonisi, V.M. Ramaglia, F. Ventriglia, Phys. Rev. B 68 (2003) 224424.
[29] C. Kwon, M.C. Robson, K.-C. Kim, J.Y. Gu, S.E. Lofland, S.M. Bhagat, Z. Trajanovic, M. Rajeswari, T. Venkatesan, A.R. Kratz, R.D. Gomez, R. Ramesh, J. Magn. Magn. Mater. 172 (1997) 229–236.